Atmos. Chem. Phys. Discuss., 13, 11997–12032, 2013
www.atmos-chem-phys-discuss.net/13/11997/2013/
doi:10.5194/acpd-13-11997-2013

Atmospheric Chemistry and Physics Discussions

Anthropogenic forcing of shift in precipitation in Eastern China in late 1970s

T. Wang[1], H. J. Wang[1,2,*], O. H. Otterå[3,6], Y. Q. Gao[1,4,6], L. L. Suo[4,6], T. Furevik[5,6], and L. Yu[5,6]

[1]Nansen-Zhu International Research Center, Institute of Atmospheric Physics, Chinese Academy of Sciences, Beijing 100029, China
[2]Climate Change Research Center, Chinese Academy of Sciences, Beijing 100029, China
[3]Uni Climate, Uni Research, Bergen, Norway
[4]Nansen Environmental and Remote Sensing Center, Bergen, Norway
[5]Geophysical Institute, University of Bergen, Bergen, Norway
[6]Bjerknes Centre for Climate Research, Bergen, Norway
[*]now at: Nansen-Zhu International Research Center, Institute of Atmospheric Physics, Chinese Academy of Sciences, Beijing 100029, China

Received: 20 January 2013 – Accepted: 11 April 2013 – Published: 7 May 2013

Correspondence to: H. J. Wang (wanghj@mail.iap.ac.cn)

Published by Copernicus Publications on behalf of the European Geosciences Union.

Abstract

Observation shows that eastern China has experienced an interdecadal shift in the summer precipitation during the second half of the 20th century. The summer precipitation increased in the middle and lower reaches of the Yangtze River Valley, whereas it decreased in northern China. Here we use a coupled ocean–atmosphere general circulation model and multi-ensemble simulations to show that the interdecadal shift is mainly caused by the combined effect of increasing global greenhouse gases and regional aerosol emissions over China. The rapidly increasing greenhouse gases induce tropical warming and a westward shift of the western Pacific subtropical high, leading to more precipitation in Yangtze River Valley. At the same time the aerosol cooling effect over land contributes to a reduced summer land–sea thermal contrast and therefore to a weakened East Asian summer monsoon and to drought in northern China. Consequently, an anomalous precipitation pattern starts to emerge in eastern China in late 1970s. Our results highlight the important role of anthropogenic forcing agents in shaping the weakened East Asian summer monsoon and associated anomalous precipitation in eastern China.

1 Introduction

The East Asian summer monsoon (EASM) leads to heavy rainfall in June, July and August along thousands of kilometers long rain belts affecting the East Asian countries, encompassing one third of the world's population. In fact, EASM contributes as much as 40–50 % (60–70 %) of the annual precipitation in the southern China (northern China) (Ding, 1992; Gong and Ho, 2003). Observations show that the EASM has experienced a significant weakening during the second half of the 20th century (Wang, 2001, 2002). This noticeable weakening concurred with more summer rainfall in the middle and lower reaches of the Yangtze River Valley (YRV) and less rainfall in northern China (Gong and Ho, 2002; Zhai et al., 2005). This interdecadal variation of the

summer precipitation (IVSP) has been referred to as the southern flood and northern drought pattern (Ding et al., 2008, 2009; Zhao et al., 2010). The weakening of the EASM and the associated IVSP have large impacts on agriculture, water resources and society for near one billion people in particularly eastern China with dense population and concentrated industries and agricultures (Piao et al., 2010). Despite the critical importance of the weakened EASM and the IVSP for China, the ultimate causes for this interdecadal shift remain unclear (Ding et al., 2009; Bollasina et al., 2011; Zuo et al., 2012).

Both natural (e.g. volcanoes) and anthropogenic (greenhouse gases and tropospheric aerosols) factors can affect the global and regional climate. For instance, a significant global reduction in precipitation over land following the Mount Pinatubo eruption in 1991 has been documented (Trenberth and Dai, 2007). Evidence from paleo proxy reconstructions also suggests a link between volcanic eruptions and decreased summer precipitation in China over the past five centuries (Shen et al., 2008). A recent study suggested that volcanic eruptions can impact the Pacific Decadal Oscillation (PDO) (Wang et al., 2012), which is a key factor to affect global and regional climate on decadal time scale (Mantua and Hare, 2002; Wang et al., 2007; Zhu et al., 2011). The rapidly increasing concentrations of atmospheric greenhouse gases also have strong impacts on the climate. According to the fourth assessment report of the IPCC (IPCC AR4), most of the observed increase in global average temperature since the mid-20th century is very likely due to the increase in greenhouse gas concentrations (Hegerl et al., 2007). It is also well known that the increase in tropospheric aerosols during the same period has produced a substantial cooling, particularly over land, and that this cooling could have reduced greenhouse gases induced warming by as much as 50 % during the 20th century (Huber and Knutti, 2012). Additionally, high tropospheric aerosol concentrations can slow down the tropical meridional overturning circulation and decrease regional summer precipitation in South Asia (Bollasina et al., 2011).

The reasons for the weakening of the EASM and the accompanying IVSP in eastern China are still not fully understood due to the complex nature of the EASM system

(e.g. land-sea thermal contrast, western Pacific subtropical high, topography) and the mixture of diverse forcing agents (Ding and Chan, 2005). It is difficult for observational studies alone to fully address all these issues, therefore the combination of in-situ data, atmosphere reanalysis data and modeling studies, becomes essential in order to understand the causes and governing mechanisms behind the weakening of the EASM. However, the IPCC AR4 models and other ensemble simulations have so far generally failed to reproduce the observed IVSP in eastern China during the late 20th century (Jiang and Wang, 2005; Meehl et al., 2008; Bollasina et al., 2011). Therefore, it is still under debate to what extent the recent observed IVSP in eastern China is caused by natural climate variability, human activities, or both.

In this study, we assess the relative roles of anthropogenic forcings and natural forcings in forming the IVSP using multi-ensemble simulations driven by different combinations of forcing agents. In Sect. 2 we describe the model and experiment design, whereas the observational and simulated interdecadal climate changes in eastern China are investigated in Sect. 3. The paper is concluded with a summary and discussion in Sect. 4.

2 Model, experimental design and data

2.1 Model

The climate model used in this study is an updated version of the Bergen Climate Model (BCM) (Furevik et al., 2003), a global, coupled atmosphere–ocean–sea-ice general circulation model (GCM). The atmosphere component is the spectral atmospheric GCM ARPEGE (Déqué et al., 1994). In this study, ARPEGE is run with a truncation at wave number 63 (T_L63), and a time step of 1800 s. A total of 31 vertical levels are employed, ranging from the surface to 10 hPa. The physical parametrization is divided into several explicit schemes, each calculating the flux of mass, energy and/or momentum due to a specific physical process (Furevik et al., 2003). The ocean component

is MICOM (Bleck and Smith, 1990; Bleck et al., 1992), a global isopycnic coordinate ocean GCM. With the exception of the equatorial region, the ocean grid is almost regular with a horizontal grid spacing of approximately 2.4° × 2.4°. In order to better resolve the dynamics near the equator, the horizontal spacing in the meridional direction is gradually decreased to 0.8° along the equator. The model has a stack of 34 isopycnic layers in the vertical, with potential densities ranging from 1029.514 to 1037.800 $kg\,m^{-3}$, and a non-isopycnic surface mixed layer on top providing the linkage between the atmospheric forcing and the ocean interior. The sea-ice model is GELATO, a dynamic-thermodynamic sea-ice model that includes multiple ice categories (Salas-Melia, 2002). The OASIS (version 2) coupler (Terray and Thual, 1995; Terray et al., 1995) has been used to couple the atmosphere and ocean models.

The model is run without any flux adjustments. The pre-industrial control simulation reproduces the major features of the global climate, and is stable for several centuries (Otterå et al., 2009).

2.2 Experimental design

The external forcings used in this study include the natural forcings (total solar irradiance and volcanoes) and the anthropogenic forcings (well-mixed greenhouse gases and tropospheric sulphate aerosols). The total solar irradiance forcing (Fig. 1) (Crowley et al., 2003) is incorporated as variations in the effective solar constant in the BCM. This modifies the top of the atmosphere short-wave flux in the BCM. The volcanic aerosol forcing (Fig. 1) (Crowley et al., 2003) includes the monthly optical depths at 0.55 µm in the middle of the visible spectrum in four bands (90°–30° N, 30° N–equator, equator–30° S and 30°–90° S). The aerosol loading was distributed in each stratospheric model level using a weighting function (Otterå, 2008). The volcanic mass of the stratospheric aerosols were then calculated at each grid-point and model level in the stratosphere by dividing the total aerosol concentration by the total air mass of all stratospheric levels at that grid point. The tropospheric sulphate aerosol forcing fields (Fig. 2) are based on the simulation of the historical sulfur cycle as prepared

for the IPCC AR4 (Lefohn et al., 1999; Boucher and Pham, 2002). In the current version of BCM only the direct effect and first indirect effect of tropospheric sulphate aerosol have been included. The horizontal distribution of the other troposphere aerosol species are held constant at their default values which are defined according to Tanre et al. (1984). The changes in the well-mixed greenhouse gases are taken from the forcing data set prepared for the EU project ENSEMBLES (Fig. 3) (Johns et al., 2011). This forcing data set includes the annual concentrations of the five most important trace gases (i.e. CO_2, CH_4, N_2O, CFC-11 and CFC-12) for the period 1850–1999 (http://www.cnrm.meteo.fr/ensembles/public/results/results.html).

Here, we use ensemble model simulations to investigate the relative importance of anthropogenic and natural forcing factors to the recent shift in precipitation and associated climate changes in eastern China. Four sets of historical simulations covering the period from 1850 to 1999 were carried out: (i) ALL150, a five-member ensemble with changes in both natural forcing agents (solar variations and volcanoes) and anthropogenic forcing agents (well-mixed greenhouse gases and tropospheric sulphate aerosols) included; (ii) ANT150, a five-member ensemble with the anthropogenic forcing agents only; (iii) NAT150, a five-member ensemble with the natural forcing agents only; and (iv) CTL150, a five-member ensemble with no year-to-year variations in the external forcing agents and with greenhouse gas and tropospheric sulphate aerosol concentration fixed at pre-industrial (1850) levels. Since the focus of this study has been to address the causes of the observed IVSP in eastern China during the late 20th century, we have restricted our model analysis to the period 1958 to 1995.

The initial conditions for ALL150, ANT150 and NAT150 were taken from a 600 yr historical simulation forced by natural variations (Otterå et al., 2010). The initial conditions for CTL150 were taken from a 600 yr pre-industrial control run (Otterå et al., 2009). Each experiment consists of five ensemble members, where each member was initialized using the common method of taking different atmosphere, but identical ocean, start conditions for the model (Collins et al., 2006). Due to the highly chaotic nature of the atmospheric model, each realization is statistically independent after only few

weeks of integration. In our case, the different atmospheric initial conditions for these four sets of simulations were generated from a previous 20 day simulation using a daily restart file every five days. This perturbation methodology is in no way optimal in terms of, for example, sampling the likely range of subdecadal atmosphere–ocean analysis error. However, it is sufficient to generate ensemble spread on the timescales of interest here.

2.3 Data

In this study, two sets of observed precipitation and surface air temperature were analyzed. One is the observed data from 740 meteorological stations (STN) collected by the China Meteorological Administration (CMA); the other is the Climate Research Unit (CRU) dataset (Mitchell and Jones, 2005). In addition, the observed data from the Hadley Centre Sea Level Pressure dataset (HadSLP2) (Allan and Ansell, 2006), the Hadley Centre monthly Sea Surface Temperature dataset (HadISST) (Rayner et al., 2003), the Extended Reconstructed Sea Surface Temperature dataset (ERSST, version v3b) (Smith et al., 2008), the National Centers for Environmental Prediction/National Center for Atmospheric Research (NCEP/NCAR) reanalysis data (Kalnay et al., 1996), and the European Centre for Medium-range Weather Forecast (ECMWF) 40 yr Reanalysis (ERA-40) (Uppala et al., 2005) were also used to evaluate model performance and to investigate interdecadal climate changes over eastern China during the second half of the 20th century.

For the statistical analyses, significance levels were calculated using a standard *t* test in this study. The Mann–Kendall test (Mann, 1945) was used to estimate the statistical significance of the linear trends. The Pearson's linear correlation coefficient was used to describe the significance of the correlation coefficients between the data and model.

3 Results

3.1 Evaluation of the model's climatology

We first examine whether BCM can reproduce observed East Asian summer climatology. Figure 4 shows that the BCM ALL150 ensemble can simulate the large scale summer precipitation and wind fields at 850 hPa reasonable well for the period of 1958–1995. There are positive-precipitation biases over South China and West China in the BCM, but model biases are small over eastern China which is our region of interest. Overall, the model is able to reproduce the spatial pattern of East Asian summer climate fairly realistic and should therefore constitute a good starting point to address the weakened EASM and the IVSP in eastern China.

3.2 The observational and simulated changes in summer precipitation

It can be seen that the precipitation increases significantly over the middle and lower reaches of the YRV, whereas it decreases over the North China and along the coasts of South China from the period 1958–1977 to the period 1978–1995 (Fig. 5). The simulated precipitation pattern in ALL150 qualitatively matches the observed anomalous precipitation pattern, but the magnitude of the precipitation anomaly in the model is less than those in the STN and CRU datasets. ALL150 also reproduces realistic precipitation anomalies in most other regions of China and adjacent areas. In contrast, neither of the ANT150 and NAT150 are able to capture the observed changes in summer precipitation over eastern China. In NAT150, negative precipitation anomalies appear over central China and northern parts of East Asia continent, which are opposite to the observation. Although shifted in a northwestward direction compared to ALL150, the negative–positive–negative precipitation anomalies do appear in ANT150, indicating linkages between the anthropogenic forcing agents and the change in the observed precipitation.

The time evolution of observed summer precipitation shows an interdecadal shift at the end of the 1970s, with drier conditions in the North China (NC, 35°–40° N, 112°–122° E) and wetter conditions in the YRV (27°–33° N, 106°–122° E, boxes in Figs. 4 and 5) for the latter two decades (Fig. 6). The STN data shows linear trends of $-0.85\,\mathrm{mm\,day^{-1}\,(40\,yr)^{-1}}$ for the NC and $1.24\,\mathrm{mm\,day^{-1}\,(40\,yr)^{-1}}$ for the YRV, which are both statistically significant at the 99 % confidence level ($P < 0.01$). Comparable trends are also seen in the CRU dataset.

The ALL150 captured the interdecadal changes in the precipitation over eastern China although linear trends are weaker, $-0.51\,\mathrm{mm\,day^{-1}\,(40\,yr)^{-1}}$ ($P < 0.01$) and $0.41\,\mathrm{mm\,day^{-1}\,(40\,yr)^{-1}}$ ($P < 0.01$) for the NC and YRV, respectively. The correlation coefficients between the STN and ALL150 reach 0.38 ($P = 0.02$) for the NC and 0.35 ($P = 0.03$) for the YRV, respectively. The other individual ensembles fail to capture the observed trend and variability. In NAT150 the precipitation trends for the NC and YRV regions are actually reversed compared to the observations. Furthermore, we examined the linear trends of observed and simulated summer precipitation over the NC and YRV during different periods (Fig. 7), focusing on the interdecadal scale (~ 40 yr). ALL150 reproduced realistic temporal evolution of interdecadal precipitation trends for these two regions through the 20th century compared with the CRU dataset. ANT150 also simulated similar temporal evolution of interdecadal precipitation trends during the second half of the 20th century, particularly for the precipitation over the YRV region, further suggesting that the IVSP in late 1970s is likely controlled by anthropogenic factors. In order to minimize the likelihood of stochastic internal variability being the cause for the opposite trends in the NC and YRV regions, we have picked the period with largest trend differences in the CTL150 simulations. For the model years 36–73 trends are $-0.34\,\mathrm{mm\,day^{-1}\,(40\,yr)^{-1}}$ for the NC ($P = 0.03$) and $0.29\,\mathrm{mm\,day^{-1}\,(40\,yr)^{-1}}$ for the YRV ($P = 0.10$). Although the anomalous pattern of the IVSP is much weak in CTL150 than in ALL150 (Fig. 5f and Fig. 6), it still implies that the internal variability of the climate system could lead to similar IVSP in eastern China. Thus, this simulated IVSP during the model years of 36–73 in CTL150 is used as parallel analysis to investigate

the differences and similarities of the IVSP and associated climate change in the East Asia between the observations and simulations.

3.3 Changes in monsoon circulation

The weakening of the Asian monsoon circulation has been suggested to be an important factor for the interdecadal precipitation shift over eastern China in the late 1970s (Ding et al., 2009). We here examined some key aspects of the observed and simulated EASM circulation for the late 20th century. In the observations, significant positive SLP anomalies are evident over East Asia, while slightly negative anomalies can be seen over the northwestern Pacific and high-latitude regions (Fig. 8a). In the reanalysis datasets, the positive SLP anomalies in NCEP/NCAR reach 6 hPa (Fig. 8b), which are much larger than those from the observation (1.2 hPa) and ERA40 (3 hPa, Fig. 8c). The ERA40 data is more consistent with observations than the NCEP/NCAR data. The large scale anomalies in SLP lead to anomalous northerly winds over eastern China (Fig. 9a and b). At the same time, both the southwestern flow from South Asia and the cross-equatorial flow from Southeast Asia are weakened, implying a weaker Asian summer monsoon circulation during the period 1978–1995. It should be noted that the changes in the wind fields are much larger in the NCEP/NCAR data than those in the ERA40 data, as should be expected from the anomalously large, positive SLP values in the NCEP/NCAR data compared with observations. The NCEP/NCAR data overestimates the interdecadal changes over Asia, as indicated by Wu et al. (2005). However, both NCEP/NCAR and ERA40 illustrate significantly weakened EASM during the period 1978–1995 relative to the period 1958–1977.

In the model, ALL150 realistically reproduced the increased SLP over the Asian continent and the weakened Asian summer monsoon circulations. These observed climatic features were partly captured by ANT150. In contrast, NAT150 failed to reproduce these climate changes. In CTL150, the weakened EASM can be found when the similar IVSP happens in eastern China. However, this interdecadal shift in summer circulation is mainly caused by the anomalous negative SLP over the South China Sea,

rather than the increased SLP over the Asian continent as found in the observations, ALL150 and ANT150.

Generally, the intensity of the EASM is controlled by the thermal contrast between land and ocean (Webster, 1987; Tao and Chen, 1987). In the observations, strong negative temperature anomalies are found over eastern China (Fig. 10a and b), with positive temperature anomalies in the surrounding regions. This distribution of temperature anomalies has been suggested to reduce meridional and zonal land–sea thermal contrasts and by that to weaken the EASM (Zuo et al., 2012).

Unlike the observations, the simulated anomalous temperature pattern in NAT150 shows large-scale cooling over East Asia for the period 1978–1995 (Fig. 10e), likely as a result of the El Chichon and Mount Pinatubo volcanic eruptions in 1982 and 1991, respectively (Fig. 11). Together with the Agung eruption in 1963, these strong volcanic eruptions in the second half of the 20th century mitigated the greenhouse gases induced warming. In CTL150, positive temperature anomalies are evident over the Indo–China Peninsula and the South China Sea, which is corresponding to the negative SLP anomalies there and lead to reduced meridional thermal contrast between land and ocean. Compared to the observations, it is suggested that neither the natural forcings nor the intrinsic climate variability alone could have caused such strong warming over East Asia and adjacent ocean.

In ALL150, on the other hand, the simulated temperature anomaly-pattern qualitatively matches the observations (Fig. 10c). According to ANT150 (Fig. 10d), the significant warm anomalies over East Asia and the surrounding oceans are presumably caused by increased greenhouse gas concentrations. Furthermore, the slight cooling in ALL150 (the less pronounced warming in ANT150) over eastern China is most likely attributed to the cooling effect of increased anthropogenic sulphate aerosols there. Unlike the greenhouse gases, the distribution of anthropogenic aerosols is spatially uneven and usually centered over industrial area such as eastern China (Fig. 2). Our results confirm that the dimming effect of rapidly increasing anthropogenic aerosols could have played an important role in the cooling trend over eastern China after 1980 (Kaiser

and Qian, 2002). As a result of the anomalous spatial temperature patterns reduced land–sea thermal contrasts are simulated over East Asia in ALL150 and ANT150. Particularly when all the external forcings are included (i.e. ALL150), the model is able to simulate more realistic changes in the surface air temperature. As a result, the EASM weakened and by that the water vapor transport cannot reach the NC, thereby causing the observed decrease in summer precipitation.

3.4 Changes in western Pacific subtropical high

The western Pacific subtropical high (WPSH) is another important component of the EASM system (Tao and Chen, 1987). The low-level jet along the western edge of the WPSH transports large amount of water vapor into East Asia. Therefore, any changes in the WPSH would potentially influence precipitation over eastern China (Ninomiya and Kobayashi, 1999). Following Zhou et al. (2009), the climatological isoline (geopotential height at 500 hPa) for the whole period (1958–1995) straddling the longitude of 130° E is defined as the characteristic WPSH isoline. As shown in Fig. 12, the black lines indicate the climatological position of the WPSH in the reanalysis datasets and numerical experiments, and their values of WPSH isoline are shown at the upper right corner. The red lines and blue lines indicate the positions of the WPSH during the periods of 1978–1995 and 1958–1977 (56–73 and 36–55 for CTL150).

Since the late 1970s, the WPSH has extended further west compared with the 1960s and 1970s. This significant interdecadal shift is also observed in the variation of the WPSH index (Fig. 13), which is defined as normalized anomalies of geopotential height at 500 hPa over the region (125°–140° E, 20°–25° N, He and Gong, 2002). As a result, the monsoon rainbelt has been pushed toward the middle and lower reaches of the Yangtze River Valley, resulting in more precipitation in this region (Gong and Ho, 2002; Zhou and Yu, 2005). Both in ALL150 and ANT150, the simulated WPSH is pushed more westward in the latter decades of the 20th century (Figs. 12 and 13), although both simulations exaggerate these changes compared with the reanalysis dataset. In

addition, the interdecadal shift in ANT150 happens earlier than that in the observations and ALL150 (Fig. 13).

Based on the previous studies (Gong and Ho, 2002; Zhou et al., 2009), the changes in the WPSH are possibly caused by the Indian Ocean–western Pacific warming during the second half of the 20th century. As shown in the observed sea surface temperature (SST) (Fig. 14), significant basin-wide SST warming can be found in the Indian Ocean and tropical Pacific during the period 1978–1995. In addition, a warm PDO like SST pattern emerged in the North Pacific during this period. Large-scale anomalously negative SSTs are evident over the west-central North Pacific, whereas positive SSTs are located over the high-latitude North Pacific and along the west coast of North America. In the BCM, these observed differences in the SST warming–cooling conditions are captured by ALL150. Forced by all the external agents, the BCM realistically reproduced the North Pacific SST decadal variation and the Indian Ocean persistent warming over the past few decades. Corresponding to the west extending of the WPSH in ALL150 and ANT150, the significant tropical warming is only evident in these two ensembles, further confirming the strong linkage between the observed changes in WPSH and persistent tropical warming during the late 20th century. Our model results suggest that the increased greenhouse gas concentration is the reason for the changes in WPSH and the tropical warming. In fact, the natural forcings also play an important role to regulate the strength of the WPSH (Fig. 13c), but its impact on the interdecadal scale is relatively small during the late 20th century. Therefore, natural forcing or intrinsic climate variability is incapable to cause such observed large-scale changes in the SST and atmospheric circulation during the second half of the 20th century (Figs. 12–14).

4 Summary and discussion

The model results presented here, together with observations, suggest that anthropogenic forcings are likely the prime drivers for the IVSP over eastern China in late 1970s. The cooling effect of the anthropogenic aerosols during the period 1958–1995

contributed to a reduced land–sea thermal contrast, leading to a weakened EASM and drought in northern China. At the same period, the greenhouse gases induced tropical warming causing a westward shift of the WPSH, which ultimately led to enhanced water vapor transport and summer precipitation over the YRV region. Consequently, the IVSP started to emerge in eastern China.

Additionally, it is found that the IVSP and similar interdecadal climate shift occur earlier in ANT150 relative to ALL150 and observations (Fig. 15). The linear trends are $-0.24\,\mathrm{mm\,day^{-1}\,(40\,yr)^{-1}}$ for the NC ($P = 0.10$) and $0.49\,\mathrm{mm\,day^{-1}\,(40\,yr)^{-1}}$ for the YRV ($P = 0.01$) during the period of 1953–1990. We therefore speculate that the natural forcings play an important role in postponing the anthropogenic forced climate changes in ALL150. This postponement could have been caused by the delayed occurrence of realistic temperature anomalies over eastern China and westward shift of the WPSH due to the cooling effects of volcanic aerosols. The model results therefore clearly underline the need to include all relevant anthropogenic and natural forcings in order to get the correct timing of the simulated shift in the East Asian climate over the past few decades. Moreover, the simulated responses in the different forced ensembles cannot be added together linearly, suggesting that complex non-linear processes are likely involved in the atmospheric response to all relevant anthropogenic and natural forcings.

Recently, Chen et al. (2012) used an atmosphere model forced by observed historical SSTs and fixed emissions scenarios at the 1990 level to reproduce a similar precipitation trend over eastern China, but their results are not able to separate the effects of the anthropogenic and natural forcings. However, Chen et al. (2012) still highlights the important role of anomalous SST forcing on the East Asian summer precipitation, as pointed out by Wang and Yan (2011) and Wang and Wang (2013). Additionally, the significant statistical relationship between the PDO and dry/wet variation of northern China in the observation (Ma and Shao, 2006) and BCM 600-yrs control run (L. Yu et al., personal communication, 2013), implies that the influence from the PDO on the precipitation in eastern China is not negligible. It means that the shifting of the PDO into

positive phase duing the late 20th century could further contribute to the drying condition in northern China, which explains the weak NC drying when none PDO signals in ANT150 (Fig. 15a and e). In our model results, the BCM does in fact a remarkable good job in reproducing the decadal SST variability over the North Pacific (i.e. PDO) and the tropical warming during the second half of the 20th century (Fig. 14c). This may be a key reason why the BCM ALL150 ensemble can successfully reproduce the weakened EASM and the IVSP over eastern China during the late 20th century. A more detailed study on the IVSP and its relation to PDO and external forcings over the 20th century will be submitted elsewhere, and will therefore not be discussed further here.

This study highlights the importance of greenhouse gases and anthropogenic aerosol emissions in the interdecadal changes of the East Asian climate. It should be noted that only sulphate aerosols have been included in this study. The potential effects of other reflecting aerosol species, such as nitrate aerosols, on the regional temperature evolution over the Asian continent have therefore not been considered (Liao et al., 2004; Wang et al., 2010; Li et al., 2011). This may be one reason why ALL150 and ANT150 simulate weaker interdecadal temperature and circulation changes relative to the observations over eastern China. On the other hand, absorbing aerosols, such as black carbon, also significantly impact the regional climate over China (Menon et al., 2002). These aerosols warm the air, and might also affect the large-scale circulation and hydrological cycle with significant climate effects. Therefore, a proper evaluation of the impact of different anthropogenic aerosol emissions for East Asia will be essential for predicting the evolution of the EASM over the coming decades. The next generation of climate model, with their increasingly more comprehensive treatment of tropospheric aerosols, offers a great opportunity to address this issue in more detail.

Acknowledgements. This work was supported by the Major State Basic Research Development Program of China (973 Program) under Grant No. 2009CB421406, the strategic Priority Research Program (XDA05120703, XDA05110203) of the Chinese Academy of Sciences, and Research Council of Norway through the DecCen project (Exploring Decadal to Century Scale Variability and Changes in the East Asian Climate during the last Millennium).

References

Allan, R. and Ansell, T.: A new globally complete monthly historical gridded mean sea level pressure dataset (HadSLP2): 1850–2004, J. Climate, 19, 5816–5842, 2006.

Bleck, R. and Smith, L. T.: A wind-driven isopycnic coordinate model of the North and Equatorial Atlantic Ocean, 1. Model development and supporting experiments, J. Geophys. Res.-Oceans, 95, 3273–3285, 1990.

Bleck, R., Rooth, C., Hu, D. M., and Smith, L. T.: Salinity-driven thermocline transients in a wind-forced and thermohaline-forced isopycnic coordinate model of the North Atlantic, J. Phys. Oceanogr., 22, 1486–1505, 1992.

Bollasina, M. A., Ming, Y., and Ramaswamy, V.: Anthropogenic aerosols and the weakening of the South Asian summer monsoon, Science, 334, 502–505, doi:10.1126/science.1204994, 2011.

Boucher, O. and Pham, M.: History of sulfate aerosol radiative forcings, Geophys. Res. Lett., 29, 1308, doi:10.1029/2001gl014048, 2002.

Chen, H. M., Yu, R. C., Li, J., Xin, X. G., Wang, Z. Z., and Wu, T. W.: The coherent interdecadal changes of East Asia climate in mid-summer simulated by BCC_AGCM 2.0.1, Clim. Dynam., 39, 155–163, doi:10.1007/s00382-011-1154-6, 2012.

Collins, M., Botzet, A., Carril, A. F., Drange, H., Jouzeau, A., Latif, M., Masina, S., Otteraa, O. H., Pohlmann, H., Sorteberg, A., Sutton, R., and Terray, L.: Interannual to decadal climate predictability in the North Atlantic: a multimodel-ensemble study, J. Climate, 19, 1195–1203, 2006.

Crowley, T. J., Baum, S. K., Kim, K. Y., Hegerl, G. C., and Hyde, W. T.: Modeling ocean heat content changes during the last millennium, Geophys. Res. Lett., 30, 1932, doi:10.1029/2003gl017801, 2003.

Déqué, M., Dreveton, C., Braun, A., and Cariolle, D.: The Arpege/Ifs atmosphere model – a contribution to the French community climate modeling, Clim. Dynam., 10, 249–266, 1994.

Ding, Y. H.: Summer monsoon rainfalls in China, J. Meteorol. Soc. Jpn., 70, 373–396, 1992.

Ding, Y. H. and Chan, J. C. L.: The East Asian summer monsoon: an overview, Meteorol. Atmos. Phys., 89, 117–142, doi:10.1007/s00703-005-0125-z, 2005.

Ding, Y. H., Wang, Z. Y., and Sun, Y.: Inter-decadal variation of the summer precipitation in East China and its association with decreasing Asian summer monsoon, Part 1: Observed evidences, Int. J. Climatol., 28, 1139–1161, doi:10.1002/Joc.1615, 2008.

Ding, Y. H., Sun, Y., Wang, Z. Y., Zhu, Y. X., and Song, Y. F.: Inter-decadal variation of the summer precipitation in China and its association with decreasing Asian summer monsoon, Part 2: Possible causes, Int. J. Climatol., 29, 1926–1944, doi:10.1002/Joc.1759, 2009.

Furevik, T., Bentsen, M., Drange, H., Kindem, I., Kvamst, N., and Sorteberg, A.: Description and evaluation of the Bergen climate model: ARPEGE coupled with MICOM, Clim. Dynam., 21, 27–51, 2003.

Gong, D. Y. and Ho, C. H.: Shift in the summer rainfall over the Yangtze River valley in the late 1970s, Geophys. Res. Lett., 29, 1436, doi:10.1029/2001gl014523, 2002.

Gong, D. Y. and Ho, C. H.: Arctic oscillation signals in the East Asian summer monsoon, J. Geophys. Res.-Atmos., 108, 4066, doi:10.1029/2002jd002193, 2003.

He, X. Z. and Gong, D. Y.: Interdecadal change in Western Pacific Subtropical High and climatic effects, J. Geogr. Sci., 12, 202–209, 2002.

Hegerl, G. C., Zwiers, F. W., Praconnot, P., Gillett, N. P., Luo, Y., Marengo Orsini, J. A., Nicholls, N., Penner, J. E., and Stott, P. A.: Understanding and attributing climate change, in: Climate Change 2007: the Physical Science Basis, Contribution of Working Group I to the Fourth Assessment Report of the Intergovernmental Panel on Climate Change, edited by: Solomon, S., Qin, D., Manning, M., Chen, Z., Marquis, M., Averyt, K. B., Tignor, M., and Miller, H. L., Cambridge University Press, Cambridge, UK and New York, NY, USA, 2007.

Huber, M. and Knutti, R.: Anthropogenic and natural warming inferred from changes in Earth's energy balance, Nat. Geosci., 5, 31–36, doi:10.1038/ngeo1327, 2012.

Jiang, D. B. and Wang, H. J.: Natural interdecadal weakening of East Asian summer monsoon in the late 20th century, Chinese Sci. Bull., 50, 1923–1929, doi:10.1360/982005-36, 2005.

Johns, T., Royer, J. F., Höschel, I., Huebener, H., Roeckner, E., Manzini, E., May, W., Dufresne, J. L., Otterå, O., and van Vuuren, D.: Climate change under aggressive mitigation: the ENSEMBLES multi-model experiment, Clim. Dynam., 37, 1975–2003, 2011.

Kaiser, D. P. and Qian, Y.: Decreasing trends in sunshine duration over China for 1954–1998: indication of increased haze pollution?, Geophys. Res. Lett., 29, 2042, doi:10.1029/2002gl016057, 2002.

Kalnay, E., Kanamitsu, M., Kistler, R., Collins, W., Deaven, D., Gandin, L., Iredell, M., Saha, S., White, G., Woollen, J., Zhu, Y., Chelliah, M., Ebisuzaki, W., Higgins, W., Janowiak, J., Mo, K. C., Ropelewski, C., Wang, J., Leetmaa, A., Reynolds, R., Jenne, R., and Joseph, D.: The NCEP/NCAR 40 yr reanalysis project, B. Am. Meteorol. Soc., 77, 437–471, 1996.

Lefohn, A. S., Husar, J. D., and Husar, R. B.: Estimating historical anthropogenic global sulfur emission patterns for the period 1850–1990, Atmos. Environ., 33, 3435–3444, 1999.

Li, Z. Q., Li, C., Chen, H., Tsay, S. C., Holben, B., Huang, J., Li, B., Maring, H., Qian, Y., Shi, G., Xia, X., Yin, Y., Zheng, Y., and Zhuang, G.: East Asian Studies of Tropospheric Aerosols and their Impact on Regional Climate (EAST-AIRC): an overview, J. Geophys. Res.-Atmos., 116, D00K34, doi:10.1029/2010jd015257, 2011.

Liao, H., Seinfeld, J. H., Adams, P. J., and Mickley, L. J.: Global radiative forcing of coupled tropospheric ozone and aerosols in a unified general circulation model, J. Geophys. Res.-Atmos., 109, D16207, doi:10.1029/2003jd004456, 2004.

Ma, Z. G. and Shao, L. J.: Relationship between dry/wet variation and the Pacific Decade Oscillation (PDO) in northern China during the last 100 yr, Chinese J. Atmos. Sci., 30, 464–474, 2006 (in Chinese).

Mann, H. B.: Nonparametric tests against trend, Econometrica, 13, 245–259, 1945.

Mantua, N. J. and Hare, S. R.: The Pacific decadal oscillation, J. Oceanogr., 58, 35–44, 2002.

Meehl, G. A., Arblaster, J. M., and Collins, W. D.: Effects of black carbon aerosols on the Indian monsoon, J. Climate, 21, 2869–2882, doi:10.1175/2007jcli1777.1, 2008.

Menon, S., Hansen, J., Nazarenko, L., and Luo, Y. F.: Climate effects of black carbon aerosols in China and India, Science, 297, 2250–2253, 2002.

Mitchell, T. D. and Jones, P. D.: An improved method of constructing a database of monthly climate observations and associated high-resolution grids, Int. J. Climatol., 25, 693–712, doi:10.1002/Joc.1181, 2005.

Ninomiya, K. and Kobayashi, C.: Precipitation and moisture balance of the Asian summer monsoon in 1991, Part 2: Moisture transport and moisture balance, J. Meteorol. Soc. Jpn., 77, 77–99, 1999.

Otterå, O. H.: Simulating the effects of the 1991 Mount Pinatubo volcanic eruption using the ARPEGE atmosphere general circulation model, Adv. Atmos. Sci., 25, 213–226, doi:10.1007/s00376-008-0213-3, 2008.

Otterå, O. H., Bentsen, M., Bethke, I., and Kvamstø, N. G.: Simulated pre-industrial climate in Bergen Climate Model (version 2): model description and large-scale circulation features, Geosci. Model Dev., 2, 197–212, doi:10.5194/gmd-2-197-2009, 2009.

Otterå, O. H., Bentsen, M., Drange, H., and Suo, L. L.: External forcing as a metronome for Atlantic multidecadal variability, Nat. Geosci., 3, 688–694, doi:10.1038/Ngeo955, 2010.

Piao, S. L., Ciais, P., Huang, Y., Shen, Z. H., Peng, S. S., Li, J. S., Zhou, L. P., Liu, H. Y., Ma, Y. C., Ding, Y. H., Friedlingstein, P., Liu, C. Z., Tan, K., Yu, Y. Q., Zhang, T. Y., and Fang, J. Y.: The impacts of climate change on water resources and agriculture in China, Nature, 467, 43–51, doi:10.1038/Nature09364, 2010.

Rayner, N. A., Parker, D. E., Horton, E. B., Folland, C. K., Alexander, L. V., Rowell, D. P., Kent, E. C., and Kaplan, A.: Global analyses of sea surface temperature, sea ice, and night marine air temperature since the late nineteenth century, J. Geophys. Res.-Atmos., 108, 4407, doi:10.1029/2002jd002670, 2003.

Salas-Melia, D.: A global coupled sea-ice–ocean model, Ocean Model., 4, 137–172, 2002.

Shen, C. M., Wang, W. C., Hao, Z. X., and Gong, W.: Characteristics of anomalous precipitation events over eastern China during the past five centuries, Clim. Dynam., 31, 463–476, doi:10.1007/s00382-007-0323-0, 2008.

Smith, T. M., Reynolds, R. W., Peterson, T. C., and Lawrimore, J.: Improvements to NOAA's historical merged land-ocean surface temperature analysis (1880–2006), J. Climate, 21, 2283–2296, doi:10.1175/2007jcli2100.1, 2008.

Tanre, D., Geleyn, J., and Slingo, J.: First results of the introduction of an advanced aerosol-radiation interaction in the ECMWF low resolution global model, in: Aerosols and Their Climatic Effects, edited by: Gerber, H. E. and Deepak, A., A. Deepak Publ., Hampton, Virginia, USA, 133–177, 1984.

Tao, S. Y. and Chen, L.: A review of recent research on the East Asian summer monsoon in China, in: Monsoon Meteorology, edited by: Chang, C. P. and Krishnamurti, T. N., Oxford University Press, 60–92, 1987.

Terray, L. and Thual, O.: Oasis: le couplage océan-atmosphére, La Météorologie, 10, 50–61, 1995.

Terray, L., Thual, O., Belamari, S., Deque, M., Dandin, P., Delecluse, P., and Levy, C.: Climatology and interannual variability simulated by the Arpege-Opa coupled model, Clim. Dynam., 11, 487–505, 1995.

Trenberth, K. E. and Dai, A.: Effects of Mount Pinatubo volcanic eruption on the hydrological cycle as an analog of geoengineering, Geophys. Res. Lett., 34, L15702, doi:10.1029/2007gl030524, 2007.

Uppala, S. M., Kallberg, P. W., Simmons, A. J., Andrae, U., Bechtold, V. D., Fiorino, M., Gibson, J. K., Haseler, J., Hernandez, A., Kelly, G. A., Li, X., Onogi, K., Saarinen, S., Sokka, N., Allan, R. P., Andersson, E., Arpe, K., Balmaseda, M. A., Beljaars, A. C. M., Van De Berg, L.,

Bidlot, J., Bormann, N., Caires, S., Chevallier, F., Dethof, A., Dragosavac, M., Fisher, M., Fuentes, M., Hagemann, S., Holm, E., Hoskins, B. J., Isaksen, L., Janssen, P. A. E. M., Jenne, R., McNally, A. P., Mahfouf, J. F., Morcrette, J. J., Rayner, N. A., Saunders, R. W., Simon, P., Sterl, A., Trenberth, K. E., Untch, A., Vasiljevic, D., Viterbo, P., and Woollen, J.: The ERA-40 re-analysis, Q. J. Roy. Meteorol. Soc., 131, 2961–3012, doi:10.1256/Qj.04.176, 2005.

Wang, H., Sun, J., and Fan, K.: Relationships between the North Pacific Oscillation and the typhoon/hurricane frequencies, Sci. China Ser. D, 50, 1409–1416, 2007.

Wang, H. J.: The weakening of the Asian monsoon circulation after the end of 1970's, Adv. Atmos. Sci., 18, 376–386, 2001.

Wang, H. J.: The instability of the East Asian summer monsoon-ENSO relations, Adv. Atmos. Sci., 19, 1–11, 2002.

Wang, T. and Wang, H. J.: Mid-Holocene Asian summer climate and its responses to cold ocean surface simulated in the PMIP2 OAGCMs experiments, J. Geophys. Res.-Atmos., doi:10.1002/jgrd.50287, 2013.

Wang, T., Ottera, O. H., Gao, Y. Q., and Wang, H. J.: The response of the North Pacific Decadal Variability to strong tropical volcanic eruptions, Clim. Dynam., 39, 2917–2936, doi:10.1007/s00382-012-1373-5, 2012.

Wang, T. J., Li, S., Shen, Y., Deng, J. J., and Xie, M.: Investigations on direct and indirect effect of nitrate on temperature and precipitation in China using a regional climate chemistry modeling system, J. Geophys. Res.-Atmos., 115, D00K26, doi:10.1029/2009jd013264, 2010.

Wang, Y. and Yan Z. W.: Changes of frequency of summer precipitation extremes over the Yangtze River in association with large-scale oceanic-atmospheric conditions, Adv. Atmos. Sci., 28, 1118–1128, 2011.

Webster, P. J.: The elementary monsoon, in: Monsoons, edited by: Fein, J. S. and Stephens, P. L., Wiley Interscience, New York, 3–32, 1987.

Wu, R. G., Kinter, J. L., and Kirtman, B. P.: Discrepancy of interdecadal changes in the Asian region among the NCEP-NCAR reanalysis, objective analyses, and observations, J. Climate, 18, 3048–3067, 2005.

Zhai, P. M., Zhang, X. B., Wan, H., and Pan, X. H.: Trends in total precipitation and frequency of daily precipitation extremes over China, J. Climate, 18, 1096–1108, doi:10.1175/Jcli-3318.1, 2005.

Zhao, P., Yang, S., and Yu, R. C.: Long-term changes in rainfall over eastern China and large-scale atmospheric circulation associated with recent global warming, J. Climate, 23, 1544–1562, doi:10.1175/2009jcli2660.1, 2010.

Zhou, T. J. and Yu, Y. C.: Atmospheric water vapor transport associated with typical anomalous summer rainfall patterns in China, J. Geophys. Res.-Atmos., 110, D08104, doi:10.1029/2004JD005413, 2005.

Zhou, T. J., Yu, R. C., Zhang, J., Drange, H., Cassou, C., Deser, C., Hodson, D. L. R., Sanchez-Gomez, E., Li, J., Keenlyside, N., Xin, X. G., and Okumura, Y.: Why the Western Pacific Subtropical High has extended westward since the late 1970s, J. Climate, 22, 2199–2215, doi:10.1175/2008jcli2527.1, 2009.

Zhu, Y. L., Wang, H. J., Zhou, W., and Ma, J. H.: Recent changes in the summer precipitation pattern in East China and the background circulation, Clim. Dynam., 36, 1463–1473, doi:10.1007/s00382-010-0852-9, 2011.

Zuo, Z. Y., Yang, S., Kumar, A., Zhang, R. H., Xue, Y., and Jha, B.: Role of thermal condition over Asia in the weakening Asian summer monsoon under global warming background, J. Climate, 25, 3431–3436, doi:10.1175/Jcli-D-11-00742.1, 2012.

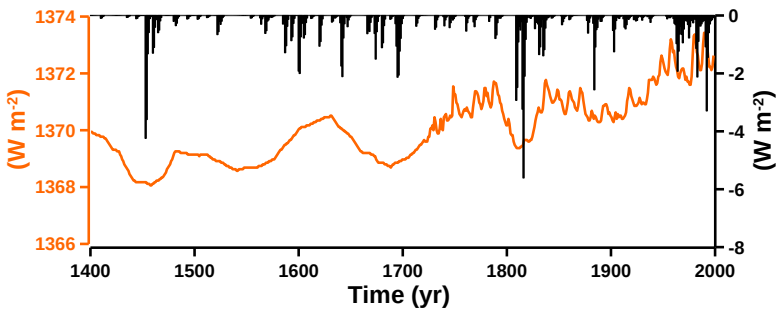

Fig. 1. Volcanic forcing (black shading) and total solar irradiance forcing (orange line) for the past 600 yr.

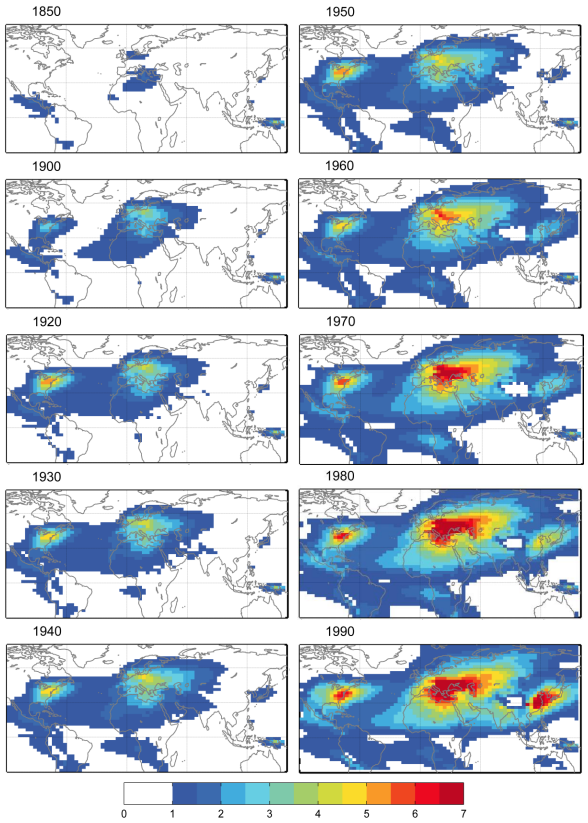

Fig. 2. Annual mean tropospheric sulphate aerosol burden ($mS\,m^{-2}$) for the years 1850, 1900, 1920, 1930, 1940, 1950, 1960, 1970, 1980 and 1990.

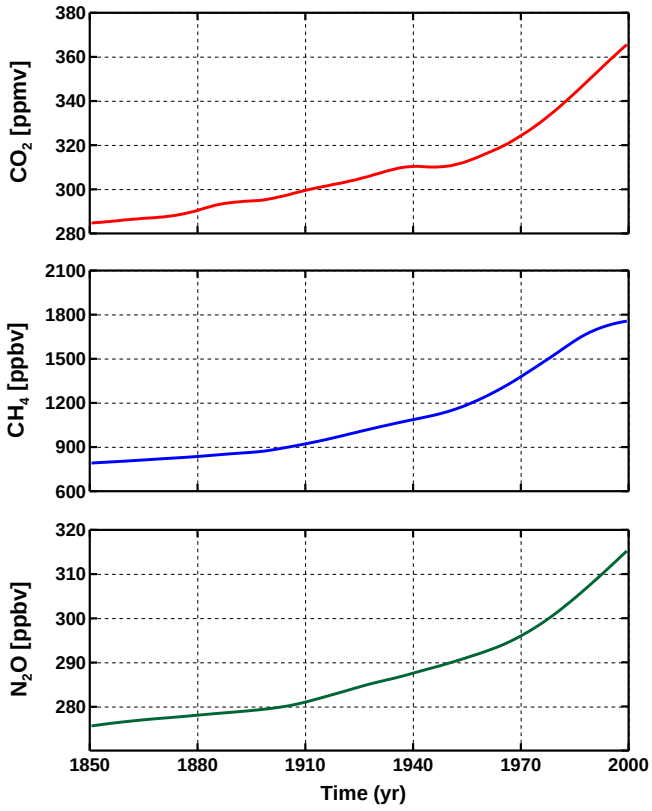

Fig. 3. Annual concentrations of three most important well-mixed greenhouse gases used to force the model for the period of 1850–1999.

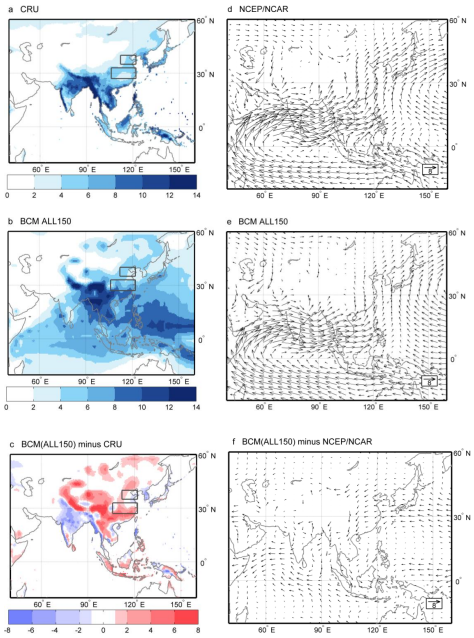

Fig. 4. Summer precipitation (June-July-August, unit: mm day^{-1}) for the period of 1958–1995 from **(a)** CRU dataset, **(b)** BCM ALL150, **(c)** BCM (ALL150) minus CRU dataset. Summer 850 hPa wind field (unit: m s^{-1}) for the same period from **(d)** NCEP/NCAR reanalysis dataset, **(e)** BCM ALL150, and **(f)** BCM (ALL150) minus NCEP/NCAR. Regions with elevations higher than 1500 m are blank. The boxes denote the analysis drought region in North China (NC, 35°–40° N, 112°–122° E) and flood region in Yangtze River Valley (YRV, 27°–33° N, 106°–122° E), over which the average precipitation trends are calculated.

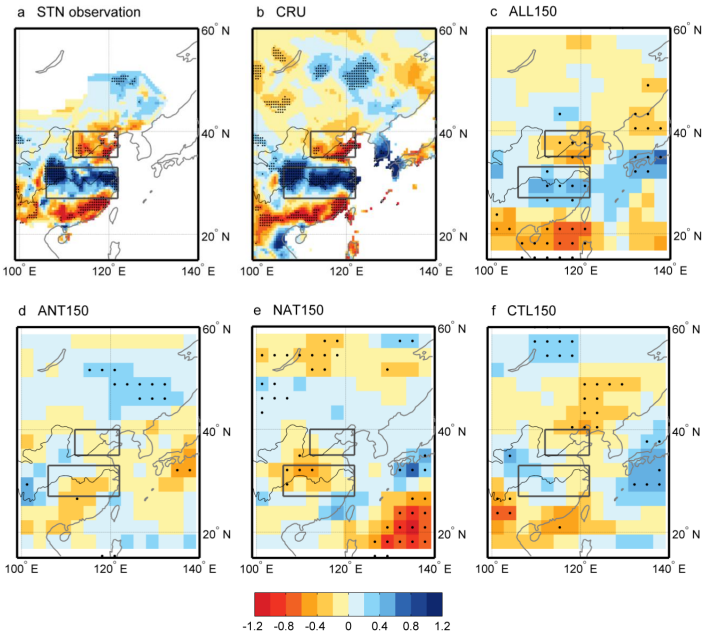

Fig. 5. The differences (1978–1995 minus 1958–1977) in summer precipitation (June-July-August, unit: mm day^{-1}) in the **(a)** STN data, **(b)** CRU dataset, **(c)** ALL150, **(d)** ANT150, and **(e)** NAT150. **(f)** The differences (56–73 minus 36–55) in the CTL150. Areas with confidence level exceeding 90 % are denoted with dots.

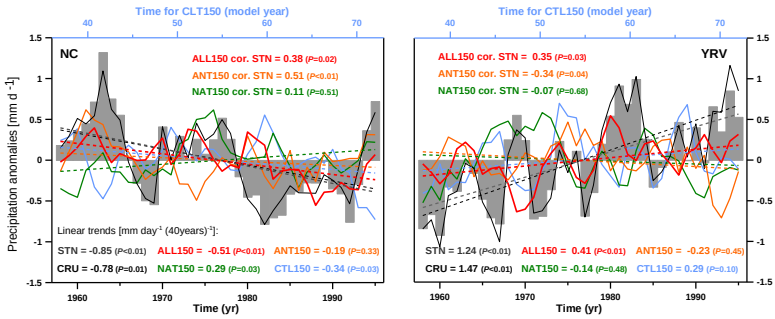

Fig. 6. Time series of 3 yr running mean summer precipitation anomalies (June-July-August, unit: mm day^{-1}) over the NC and YRV regions (see the black boxes in Fig. 5). Anomalies are calculated as deviations from the 1958–1995 (36–73 for the CTL150) climatology. The grey histograms and black lines are based on the STN and CRU TS 3.0 observational datasets, respectively. The red, orange, green and blue lines are for the ALL150, ANT150, NAT150 and CTL150 historical integrations, respectively. The least-squares linear trends during 1958–1995 (36–73 for the CTL150) are plotted as dashed lines in the respective colors.

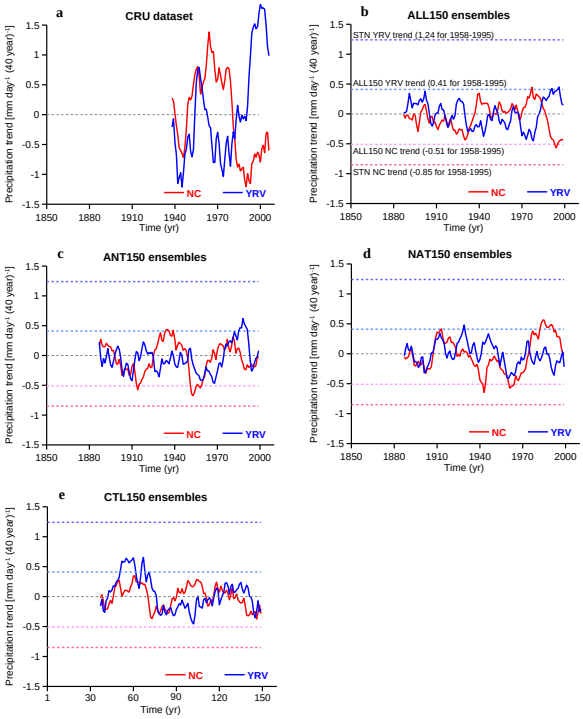

Fig. 7. Running interdecadal trends for the summer precipitation anomalies over the NC and YRV regions in the **(a)** CRU dataset, **(b)** ALL150, **(c)** ANT150, **(d)** NAT150, and **(e)** CTL150. The running window width is 38 yr, same length as the period of 1958–1995 (i.e. the value in the year 1999 represents the linear trend for the period of 1962–1999).

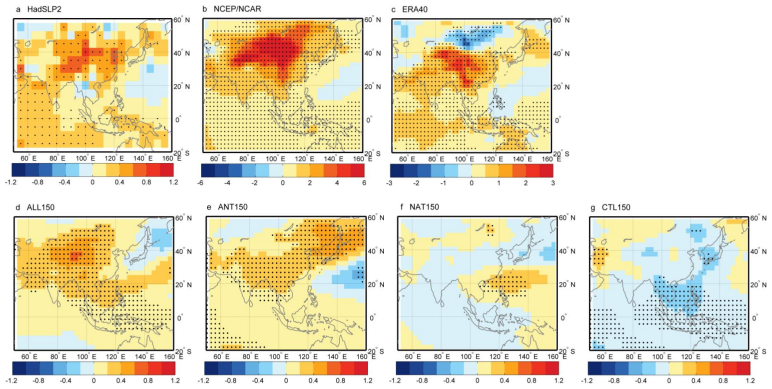

Fig. 8. The differences (1978–1995 minus 1958–1977) in summer sea level pressure (June-July-August, unit: hPa) in the **(a)** HadSLP2, **(b)** NCEP, **(c)** ERA40, **(d)** ALL150, **(e)** ANT150, and **(f)** NAT150. **(g)** The differences (56–73 minus 36–55) in the CTL150. Areas with confidence level exceeding 90 % are denoted with dots.

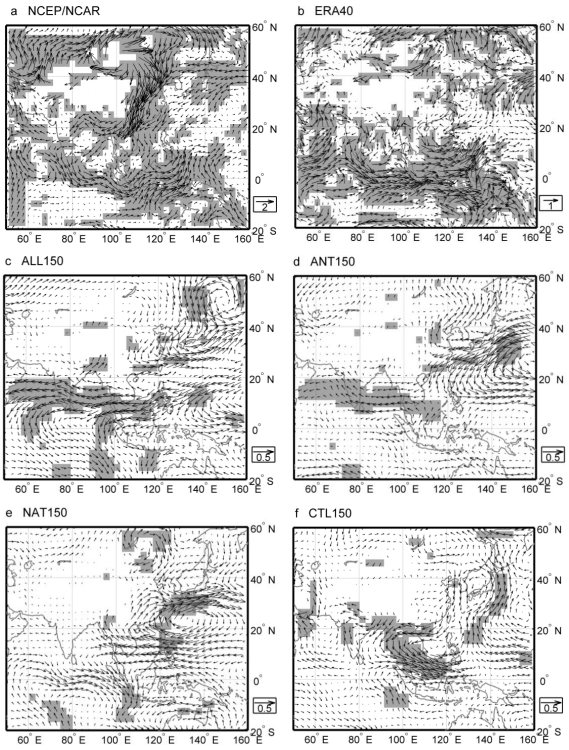

Fig. 9. The differences (1978–1995 minus 1958–1977) in summer wind fields at 850 hPa (June-July-August, unit: $m\,s^{-1}$) in the **(a)** NCEP/NCAR, **(b)** ERA40, **(c)** ALL150, **(d)** ANT150, and **(e)** NAT150. **(f)** The differences (56–73 minus 36–55) in the CTL150. Areas with confidence level exceeding 90 % are shaded with gray. Regions with elevations higher than 1500 m are blank.

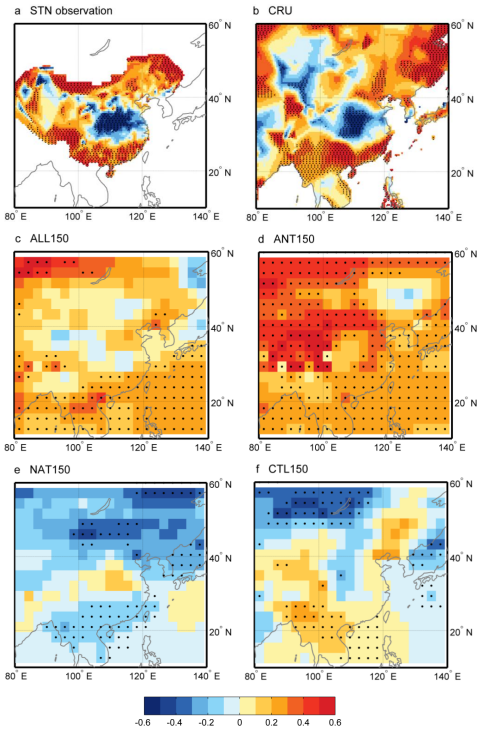

Fig. 10. The differences (1978–1995 minus 1958–1977) in summer surface air temperature (June-July-August, unit: °C) in the **(a)** STN data, **(b)** CRU dataset, **(c)** ALL150, **(d)** ANT150, and **(e)** NAT150. **(f)** The differences (56–73 minus 36–55) in the CTL150. Areas with confidence level exceeding 90 % are denoted with dots.

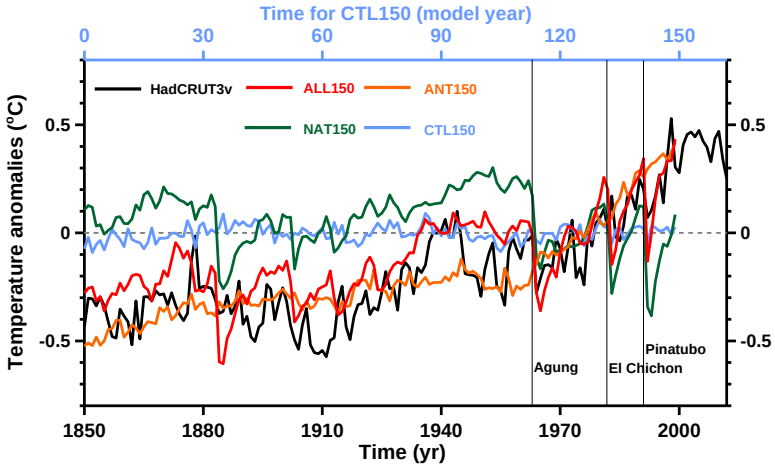

Fig. 11. Time series of the global–mean surface air temperature anomalies (unit: °C), relative to the 1961–1990 (112–141 for CTL150) average, for the HadCRUT3v observational dataset and ensemble model results.

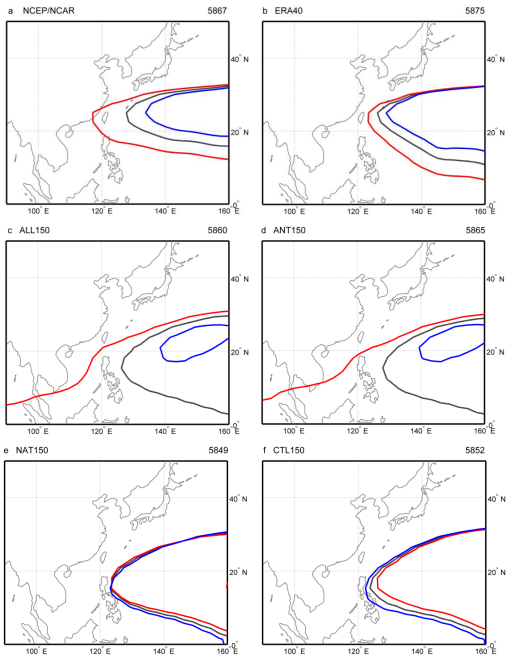

Fig. 12. The observed and simulated positions of characteristic western Pacific Subtropical High isoline at 500 hPa during the periods 1978–1995 (red line), 1958–1977 (blue line) and 1958–1995 (black line) in the **(a)** NCEP/NCAR, **(b)** ERA40, **(c)** ALL150, **(d)** ANT150, **(e)** NAT150 and **(f)** the corresponding periods (56–73, 36–55) in the CTL150. The value of the western Pacific Subtropical High isoline in each data is shown at the upper right corner (unit: m).

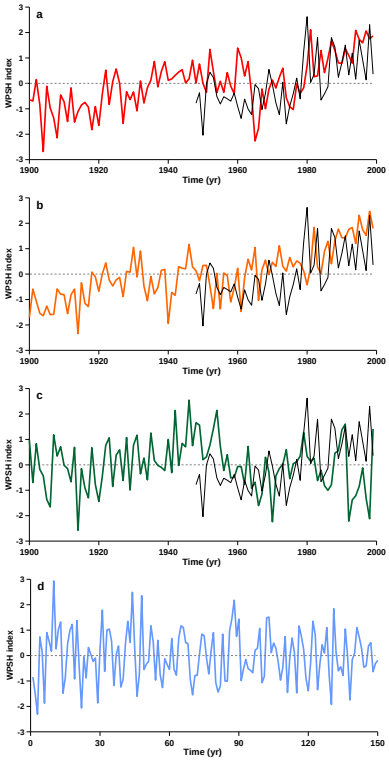

Fig. 13. Time series of simulated and NCEP/NCAR (black lines) summer western Pacific Subtropical High index (June-July-August) from **(a)** ALL150, **(b)** ANT150, **(c)** NAT150, and **(d)** CTL150.

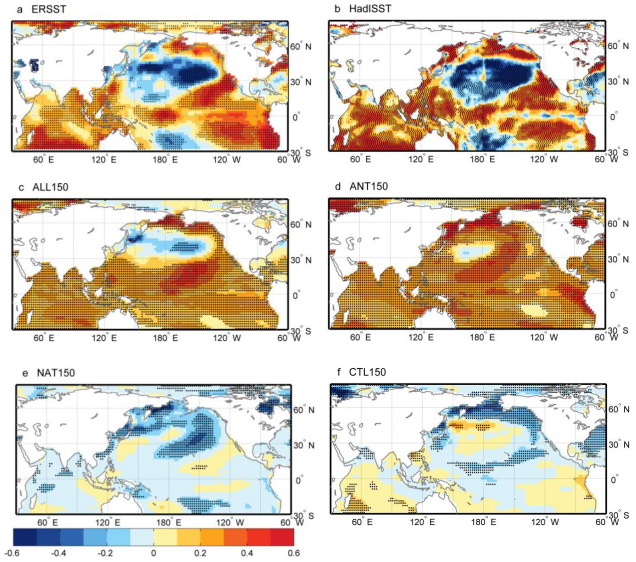

Fig. 14. The differences (1978–1995 minus 1958–1977) in the observed and simulated summer SST (June-July-August, unit: ˚C) in the **(a)** ERSST, **(b)** HadISST, **(c)** ALL150, **(d)** ANT150, and **(e)** NAT150. **(f)** The differences (56–73 minus 36–55) in the CTL150. Areas with confidence level exceeding 90 % are denoted with dots.

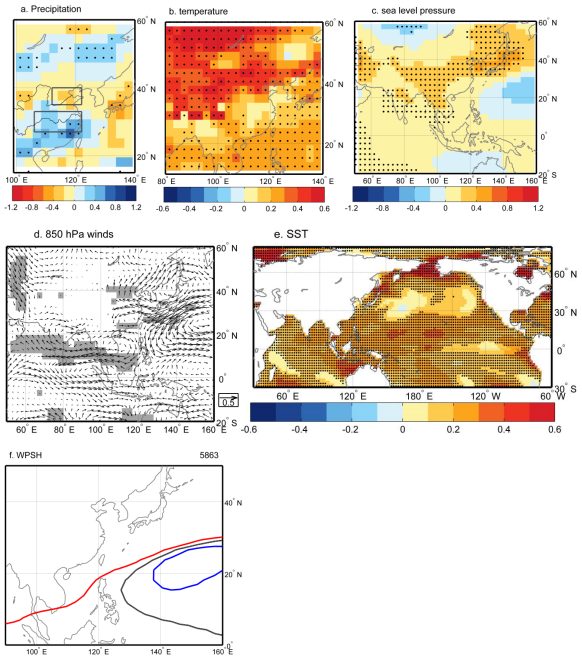

Fig. 15. ANT150 simulated differences (1973–1990 minus 1953–1972) in summer (June-July-August) **(a)** precipitation (unit: mm day^{-1}), **(b)** surface air temperature (unit: ˚C), **(c)** sea level pressure (unit: hPa), and **(d)** wind fields at 850 hPa (unit: m s^{-1}), and **(e)** SST (unit: ˚C). Areas with confidence level exceeding 90 % are denoted with dots or shaded. **(f)** The positions of characteristic western Pacific Subtropical High isoline at 500 hPa during the periods 1973–1990 (red line), 1953–1972 (blue line) and 1953–1990 (black line). The value of the western Pacific Subtropical High isoline is shown at the upper right corner (unit: m).